Geochemistry Geophysics Geosystems G3
AN ELECTRONIC JOURNAL OF THE EARTH SCIENCES
Published by AGU and the Geochemical Society

Article
Volume 9, Number 7
24 July 2008
Q07017, doi:10.1029/2008GC002022
ISSN: 1525-2027

Modeling of gas-driven magmatic overturn: Tracking of phenocryst dispersal and gathering during magma mixing

Philipp Ruprecht and George W. Bergantz
Department of Earth and Space Science, University of Washington, Box 351310, Seattle, Washington 98195, USA (ruprecht@u.washington.edu; bergantz@u.washington.edu)

Josef Dufek
Department of Earth and Planetary Science, University of California, Berkeley, 307 McCone Hall, Berkeley, California 94720, USA (dufek@berkeley.edu)

[1] We present a combined multiphase numerical and crystal-tracking approach that provides a framework to investigate the transport and zoning of crystals associated with a gas-driven mixing event. Mixing in compositionally intermediate to silicic magmatic systems is often initiated by gas exsolution in the recharging magma, causing a density inversion and subsequent overturn. The overturn is simulated for a range of bubble volume fractions $\varepsilon_{bubbles}$ and therefore indirectly for a range of Reynolds numbers *Re*. All simulations show chaotic flow dynamics with fast overturn timescales of minutes to hours. The large-scale mixing is inefficient during a single overturn, resulting in a continuously stratified system with respect to bubble volume fraction. The crystal-tracking algorithm provides us with information on the small scales, i.e., 10 cm. On this length scale we observe gathering of different crystals during the overturn that typically ranges on the order of tens of meters. Thus, a complex crystal population may arise within a single overturn. This gathering and dispersal of crystals is strongest and most uniform for high *Re*. For low *Re*, crystal populations are characterized by less gathering of crystals that originated from distal portions of the magma body. During the overturn the crystals pass through environments of changing chemical potential. We apply the Damköhler number *Da*, which compares the crystallization or dissolution to the advection timescale. Results show an asymmetry between crystallization and dissolution. Crystallization times are too slow during gas-driven overturn to record transient changes in chemical potential. Crystals most likely only record their initial as well as their final chemical environment. In contrast, dissolution and advection rates are of similar order, suggesting potential dissolution during the overturn. On the basis of the results for gas-driven overturn we expect that slower physical mixing processes may be continuously recorded in the zonation pattern of the crystal phases as long as the changes in chemical potential produce crystal growth.

Components: 11,860 words, 9 figures, 2 tables.

Keywords: magma dynamics; magma mixing; gas-driven overturn; crystal tracking; crystal zonation.

Index Terms: 3618 Mineralogy and Petrology: Magma chamber processes (1036); 3620 Mineralogy and Petrology: Mineral and crystal chemistry (1042); 8439 Volcanology: Physics and chemistry of magma bodies.

Received 6 March 2008; **Revised** 4 June 2008; **Accepted** 11 June 2008; **Published** 24 July 2008.

Ruprecht, P., G. W. Bergantz, and J. Dufek (2008), Modeling of gas-driven magmatic overturn: Tracking of phenocryst dispersal and gathering during magma mixing, *Geochem. Geophys. Geosyst.*, *9*, Q07017, doi:10.1029/2008GC002022.

1. Introduction

[2] The chemical and textural characteristics of crystals [*Singer et al.*, 1995, *Zellmer et al.*, 2003; *Ginibre et al.*, 2004; *Humphreys et al.*, 2006; *Morgan et al.*, 2007; *Davidson et al.*, 2007; *Ruprecht and Wörner*, 2007] suggest complex magmatic histories for many volcanic centers [*Davidson and Tepley*, 1997; *Bachmann et al.*, 2002; *Vazquez and Reid*, 2004]. Such case studies have shown that this heterogeneity in the crystals emerges from the in situ mixing of magmatic additions in the shallow crust [*Knesel et al.*, 1999; *Tepley et al.*, 2000; *Couch et al.*, 2001; *Coombs and Gardner*, 2004] and/or during eruption [*Cioni et al.*, 1995].

[3] A quantitative understanding of the emergence of crystal-scale heterogeneity has still to be developed. The chemical and textural information recorded in a crystal is a competition between the rate at which the crystal travels through regions of distinct chemical potential, and the rate at which the crystal can respond to those changes through crystallization or dissolution. *Wallace and Bergantz* [2005] have developed a method to identify groups of crystals that have shared some common residence history. However, their approach did not allow one to connect specific rates and paths of crystal transport with the rates at which crystals can respond to changes. Our objective is to exemplify the styles and scales of crystal dispersal and gathering to understand the controls and consequences of magma chamber dynamics as expressed in the crystal cargo.

[4] All physical processes that promote efficient large-scale mixing require advective mass flux, which is a mechanism for both stretching (which reduces diffusive length scales) and redistribution. Gravitational instabilities provide one of the primary mechanisms for mixing in systems with unstable stratification arising from thermal, compositional, or phase segregation driven buoyancy [*Jellinek et al.*, 1999]. One example is Rayleigh-Taylor instabilities such as dripping dense crystal layers [*Marsh*, 1988; *Bergantz and Ni*, 1999], superposition of silicic and/or cold magma over mafic and/or hot magma [*Oldenburg et al.*, 1989; *Snyder and Tait*, 1996; *Folch and Martí*, 1998; *Snyder*, 2000; *Bergantz and Breidenthal*, 2001; *Couch et al.*, 2001] or the injection of replenishing magma [*Jellinek et al.*, 1999; *Jellinek and Kerr*, 1999; *Phillips and Woods*, 2001; *Longo et al.*, 2006].

[5] All these models resolve some features of the large-scale or averaged behavior of the mixing process such as the bulk changes of temperature or redistribution of a gas bubble fraction. Multiphase continuum models can calculate mass and energy fluxes, and this is an essential first step in illuminating how distinct regions of temperature or composition of a magma system emerge, mix and decay. However, the progressive, transient paths of individual crystals and the local conditions that are recorded on the crystal-scale cannot be resolved with these methods alone. The emergence and evolution of different crystal populations can only be deduced by combining "smart crystals," which are Lagrangian tracers, with the temporally changing conditions for the magma chamber. These tracers are like flight recorders in the way they can probe for information at the crystal scale, and are also fully coupled physically to the flow, and so they are not simple passive tracers. This approach has been used extensively in engineering problems [e.g., *Derksen*, 2003], in which particles are dynamically responding to the local body and surface forces, and are not just tracers following the motion.

[6] Our aim is to investigate how much diversity in individual crystal zoning and crystal populations can arise from a simple kinematic template: one cycle of overturn associated with degassing from a vesiculated mafic magma that has intruded into a more silicic layer. To do this we examine the trajectory of neighboring crystal pairs after a cycle of overturn and how their transport produces regions of homogeneity and heterogeneity in a crystal population. Mixing associated with volatile exsolution from a recharging magma has been suggested as a potentially important process [*Eichelberger*, 1980]. The physical nature of such gas-driven mixing and overturn has been investigated with analog [*Phillips and Woods*, 2001], analytical [*Bergantz and Breidenthal*, 2001], and numerical techniques [*Longo et al.*, 2006].

2. Physical Model of Magma Mixing and Crystal Tracking

[7] Our objective is to explore the transport and zoning of crystals in a single episode of magma chamber overturn. Our numerical model describes the compositional mixing/hybridization caused by a gas-rich magma underlying a bubble-free magma, a condition suggested to arise in nature

Table 1. Physical Properties and Model Parameters Used in the Simulations

Description	Parameter	Value
Magma viscosity	μ_{magma}	10^4 Pa s[a]
Particle density	$\rho_{particle}$	2800 kg m^{-3}
Melt density	ρ_{melt}	2400 kg m^{-3}
Bubble density	$\rho_{bubbles}$	600 kg m^{-3}[b]
Bubble-bearing layer thickness	h	40 m
Bubble diameter	$\phi_{bubbles}$	10^{-3} m
Particle diameter	$\phi_{particle}$	10^{-3} m
Bubble volume fraction	$\varepsilon_{bubbles}$	0.02, 0.05, 0.1, 0.2, 0.3, 0.4
Critical bubble volume fraction	ε_{cp}	0.5
Cell resolution (vertical and horizontal)		0.4 m

[a] Resembles most intermediate to silicic melts [*Scaillet et al.*, 1998]. Following equation (3) and a volume balance between crystals and melt, we can calculate the effective melt viscosities. For common crystal volume fractions of 0 to 0.25 in arc magmas the effective melt viscosity remains of the same order and ranges from 7.4 to10×10^4 Pa s.
[b] Similar bubble density taken as for Pinatubo dacite [*Gerlach et al.*, 1996].

[e.g., *Eichelberger*, 1980; *Pallister et al.*, 1992; *Nakamura*, 1995]. This is a useful end-member for magma chamber overturn because it is likely one of the fastest, naturally occurring instabilities with respect to instability growth and overturn completion due to the large density variations between the gas bubbles and the magma. In our simulations we begin with a fixed bubble volume fraction in the bubble-bearing magma which is intrinsically unstable. Hence we do not attempt to model the complex and poorly understood paths to progressive vesiculation. Natural recharge events will likely have a range of mass flux and exsolved bubble-volume fraction. Our aim is not to model any particular recharge event but to explore the dynamics associated with a geologically reasonable, but end-member set of conditions.

[8] All simulations were performed under isothermal conditions because we assume that the timescale of advection of enthalpy by the overturning process is much faster than any other heat transfer process. Thus, we ignore processes such as secondary nucleation and additional gas exsolution. We simplify the natural system by assuming an identical solid and liquid composition for the bubble-free and the bubble-bearing magmas. Thus, viscosity variations arising from temperature and compositional dependence, phase transitions and bubble coalescence are ignored. In our model viscosity differences only emerge from the varying content in bubbles. In natural systems these viscosity variations may alter the kinematic template significantly and further studies including those complexities will be necessary. However, to be able to assess the individual effects of viscosity and initial density contrast we need to consider these effects separately to make progress in understanding the dynamics of magma-magma interaction on the bulk and the crystal scale. Thus, we have focused on a simple but geologically significant end-member.

[9] To resolve the complex multiphase character of natural magmas, we have divided the system into two parts each of which resolves different scales. The first and largest scale is calculated with a multiphase finite-volume approach [*Patankar*, 1980; *Gidaspow*, 1994] for a carrier phase (silicate melt plus "background" crystals) and a dispersed phase (bubbles). We assume that the "background" crystals are passively advected by the melt [*Aref*, 1990], thus treating the carrier phase as a virtual single phase whose properties can be calculated using mixture theory [*Burgisser et al.*, 2005]. We subsequently refer to this melt and crystal mixture as the magma phase. For sufficiently small crystal volume fractions, melt and magma viscosities are of similar order of magnitude (Table 1). Hence, the crystals have little effect on the kinematic template established by the fluid motion. We employ a form of the MFIX [*Syamlal et al.*, 1993] multiphase fluid code that we have modified for magma conditions. *Dufek and Bergantz* [2005, 2007] used a similar approach to investigate flow dynamics in a magmatic conduit and in a pyroclastic flow. The simulation tracks the volume fractions of the silicate melt-crystal mixture and the gas bubbles in a magmatic system that is 200 m wide and 100 m high. Different aspect ratios were not considered here. Varying aspect ratios can have a significant effect on the mixing dynamics, which is discussed as part of the overall mixing dynamics below. The width of the model was chosen to ensure that the boundaries are not affecting the flow and the width is greater than several wavelengths of the examined Rayleigh-Taylor type instabilities that dominate the most active period of the flow.

[10] For all multiphase fluid dynamics simulations the initial conditions are a 60 m thick bubble-free magma overlying a 40 m thick bubble-bearing magma. The physical properties are given in Table 1. Six simulations were performed, where the only difference was the bubble volume fraction, $\varepsilon_{bubbles}$

of, the lower bubble-rich layer. The lowest bubble volume fraction was 0.02 and the highest was 0.4.

[11] The boundaries of the system are subject to no-slip for the bottom and top wall and free-slip conditions for the sidewalls. Thus, the velocities for all phases approach zero on the horizontal boundaries, while the velocity gradients approach zero on the sidewalls:

$$v_{bottom} = v_{top} = 0, \tag{1}$$

$$\left(\frac{dv}{dx}\right)_{east} = \left(\frac{dv}{dx}\right)_{west} = 0. \tag{2}$$

These conditions are appropriate for a magma system that is sill-like and may continue horizontally.

[12] Bubbles are modeled as rigid spheres implying that bubble surface tension exceeds viscous stresses from fluid motion. Analog conduit experiments performed by *Namiki and Manga* [2006] demonstrated that even under conditions of high magmatic viscosity and high shear rates, like volcanic conduits during an eruption, bubbles maintain their spherical shape.

[13] The within-phase bubble viscosity $\mu_{bubbles}$, which is the drag of the bubbles by the other bubbles, is modeled using the relationship by [*Beckermann and Viskanta*, 1993]

$$\mu_{bubbles} = \mu_{magma}\left(1 - \frac{\varepsilon_{bubbles}}{\varepsilon_{cp}}\right)^{-2.5\varepsilon_{cp}}, \tag{3}$$

where ε_{cp} is the closed packing bubble volume fraction and μ_{magma} the dynamic magma viscosity.

[14] Once the dynamics of the overturn have been solved (as shown in Figure 1), the so-called smart crystals, or crystal recorders are imbedded in the flow.[1] In this step 20,000 crystals are randomly seeded throughout the magma system and their progress is tracked. The motion of the particles is calculated using the particle motion model of *Burgisser et al.* [2005]. The Bassinet-Boussinesq-Oseen (BBO) equation describes the force-balance for spherical particles [*Maxey and Riley*, 1983]. For most applications only the drag and body forces are of importance [*Burgisser et al.*, 2005]. In this case the horizontal and vertical component of the acceleration for each crystal can be calculated from the local melt velocity field, respectively, by

$$\frac{dv_i}{dt} = \frac{f}{\tau_v}(u_i - v_i)\left(\frac{2\rho_p}{2\rho_p + \rho_f}\right), \tag{4a}$$

$$\frac{dv_i}{dt} = \frac{f}{\tau_v}(u_i - v_i)\left(\frac{2\rho_p}{2\rho_p + \rho_f}\right) + g\left(\frac{2\rho_p - 2\rho_f}{2\rho_p + \rho_f}\right), \tag{4b}$$

where v_i and u_i are the crystal and melt phase velocities, respectively, and g, ρ_p and ρ_f are the acceleration due to gravity, crystal density and melt density, respectively. The magma velocity from the multiphase fluid model is used to approximate the melt phase velocity. As noted earlier, for sufficiently small crystal volume fractions this approximation is valid, because crystal-crystal interaction is limited [*Burgisser et al.*, 2005]. Following *Burgisser et al.* [2005] the drag coefficient f and the particle response time τ_v are defined as

$$f = 1 + 0.15\,\mathrm{Re}_p^{0.687} + \frac{0.0175}{\left(1 + 42500\,\mathrm{Re}_p^{-1.16}\right)}, \tag{5}$$

$$\tau_v = \frac{\left(\rho_p - \rho_f\right)\phi^2}{18\mu}, \tag{6}$$

with Re_P, ϕ and μ being the particle Reynolds number, particle diameter and the dynamic magma viscosity, respectively.

[15] The particle Reynolds number Re_P, which describes the kinematics of the flow regime of a melt around a particle, is given as

$$\mathrm{Re}_p = \frac{U_T\phi}{\upsilon}, \tag{7}$$

where U_T is a reference velocity taken here as the terminal fall velocity is and υ is the kinematic magma viscosity.

[16] We only track one size of crystals (1 mm) in our tracer calculations. In a scaling study on igneous processes *Burgisser et al.* [2005] showed that for conditions in a magma chamber with high melt viscosity and small particle size, the crystal response time is much shorter than the timescale of fluid motion. Hence, crystals closely follow the fluid flow. The particle response time, despite its quadratic dependence on crystal size (equation (6)), is on the order of nanoseconds. Thus, a single

[1] Auxiliary materials are available in the HTML. doi:10.1029/2008GC002022.

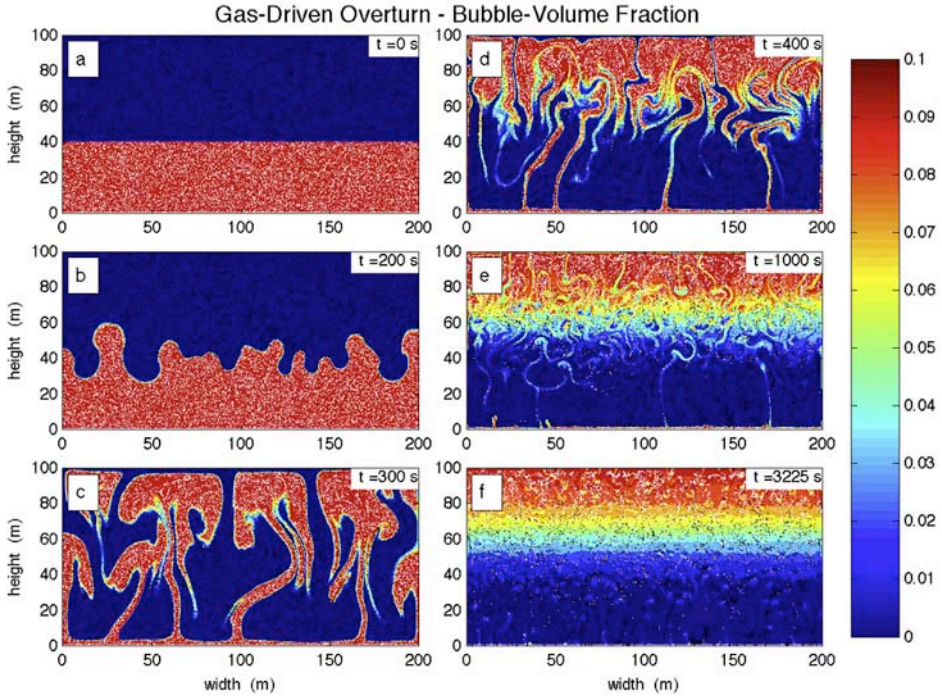

Figure 1. Different stages in the overturn of a lower, bubble-rich layer for an initial $\varepsilon_{bubbles} = 0.1$. Colors indicate $\varepsilon_{bubbles}$. White and black Lagrangian crystals refer to initially bound to the bubble-rich and bubble-poor layers, respectively. Symbols are bigger than the crystal diameter of 1 mm. Initial conditions are a 60 m thick bubble-poor layer overlying a 40 m bubble-bearing layer. East and west boundaries are free-slip, while top and bottom boundaries are nonslip. Physical properties are given in Table 1. The transient overturn is showing different generations of plumes rising through the chamber until ~1000 s. The simulation is terminated after 3225 s. A stable stratified system has developed, and average crystal velocities are smaller than 0.08 mm s^{-1}. Auxiliary material Animations 1 and 2 show the entire simulation. Animation 1 omits displaying the "smart" crystals to improve the visibility of the dynamics in the multiphase simulation.

crystal size is sufficient to track any crystal paths during the overturn.

[17] Equations (4) through (7) provide the framework to determine the trajectory of each crystal within the developing flow. The velocity field of the melt at the position of the crystal is interpolated on the basis of the calculated velocity values at the control volume interfaces. In the present model 20,000 Lagrangian particles distributed randomly over the entire magma chamber were followed for the simulation with $\varepsilon_{bubbles} = 0.1$ and $\varepsilon_{bubbles} = 0.3$, respectively (Figure 1). Crystal motions are calculated until the major overturn has ceased and the average crystal velocities are less than 0.08 mm s^{-1}.

3. Results: Overall Mixing Dynamics

[18] Given our initial conditions where there is a density gradient that is opposite to the pressure gradient, a Rayleigh-Taylor (R-T) instability forms. The governing parameters describing the evolution of an R-T instability are the Atwood number A [*Ramaprabhu and Andrews*, 2004], and the viscosity ratio μ_l/μ_u of the lower layer μ_l and the upper layer μ_u, respectively [*Ramberg*, 1981, Table 2]. The viscosity ratio is required because the Reynolds numbers are not high enough to ensure that the motion is fully turbulent with a loss of memory of initial conditions. Hence, the flow is not self-similar. The Atwood number describes the dimensionless density ratio of the two layers where

$$A = \frac{(\rho_u - \rho_l)}{(\rho_u + \rho_l)}, \tag{8}$$

and ρ_u and ρ_l refer to the density of the upper and lower layers, respectively. Much work has focused on systems with large values of A [e.g., *Youngs*, 1984]. In contrast, a more recent study by *Linden*

Table 2. Atwood Number A, Density Ratio, Viscosity Ratio, Reynolds Number Re, Overturn Timescale, and Wavelength

$\varepsilon_{bubbles}$	A	ρ_l/ρ_u	μ_l/μ_u	Re[a]	Re[b]	$t_{overturn}$[c] (hours)	λ_m[d] (m)
0.02	0.008	0.985	1.001	92	15	2.13	77.9
0.05	0.019	0.963	1.007	146	52	1.60	57.7
0.10	0.039	0.925	1.032	206	104	1.13	46.5
0.20	0.081	0.850	1.179	291	364	0.83	39.2
0.30	0.127	0.775	1.643	356	344	0.80	39.5
0.40	0.176	0.700	3.591	412	355	0.99	52.6

[a] Predicted values after *Linden and Redondo* [1991].
[b] Observed *Re* number for simulation, calculated from *Nitsche and Batchelor* [1997].
[c] Time until average velocity of "smart" crystals is smaller than 0.08 mm/s.
[d] Predicted wavelengths after *Linden and Redondo* [1991].

and Redondo [1991] employed an experimental approach to investigate a Rayleigh-Taylor instability in a system with low values of A, which are similar to values of A found in shallow magmatic systems. In our study A ranges from 2×10^{-3} to 1.8×10^{-1}.

[19] Following *Chandrasekhar* [1961] and given A and the average kinematic viscosity of the system υ we can predict the characteristic wavelength λ_m of the main plumes generated from the R-T instability using

$$\lambda_m = 4\pi\left(\frac{\upsilon^2}{gA}\right)^{1/3}, \tag{9}$$

$$\upsilon = \frac{(\mu_{melt} + \varepsilon_{bubbles}\mu_{bubbles} + (1-\varepsilon_{bubbles})\mu_{melt})}{(\rho_{melt} + \varepsilon_{bubbles}\rho_{bubbles} + (1-\varepsilon_{bubbles})\rho_{melt})}. \tag{10}$$

[20] The energy and timescale of the overturning motion is directly related to $\varepsilon_{bubbles}$. Hence we considered six different bubble volume fractions ranging from 0.02 to 0.40. The observed timescales decrease for increasing $\varepsilon_{bubbles}$ with the exception of the simulation with the largest bubble volume fraction. In the case of $\varepsilon_{bubbles} = 0.4$ the timescale is increasing, because the initial instability contains so much potential energy that the system overshoots. The viscosity is not capable of damping the overturn significantly and after the main overturn has ceased small waves are traveling through the system, keeping the average crystal velocities above our termination criterion for the simulation. The wavelength also has a minimum for $\varepsilon_{bubbles}$ between 0.2 and 0.3 after which the kinematic viscosity increases dramatically. Therefore, the characteristic wavelength of the overturning motion increases again for large-bubble volume fractions. The maximum system-wide Reynolds number (Re) for each simulation varies from 15 to 364, respectively (Table 2). It is calculated on the basis of the velocity approximation $v_{instability}$ for particle-laden blobs [*Nitsche and Batchelor*, 1997] and the diameter L of the largest plume that crosses a plane at 45 m height [*Nitsche and Batchelor*, 1997]:

$$\mathrm{Re} = \frac{v_{instability} L}{\upsilon_{magma}}, \tag{11}$$

$$v_{instability} = \frac{\left(\rho_{instability} - \rho_{magma}\right) g L^2}{3\mu_{magma}} \frac{\mu_{magma} + \mu_{instability}}{\mu_{magma} + \frac{3}{2}\mu_{instability}}, \tag{12}$$

where $\rho_{instability}$ and $\mu_{instability}$ are the mean density and viscosity of the particle-laden blobs. Here, we consider the bubbles as a separate dispersed phase of the magma, while crystals and melt are combined together as the virtual single phase. Although differing by up to one order of magnitude for the lowest bubble volume fractions from the expected values presented in the previous section, Re numbers still fall into the regime of transitional flow: not fully turbulent but unsteady. All the simulations produced a fast overturn: less than 3 hours (Table 2), with a complex dynamic template composed of an incomplete spectrum of eddy sizes in this transitional flow regime.

[21] Changing the aspect ratio or the volume of bubble-bearing magma has an immediate effect on the Reynolds number of the system, thus affecting the overturn timescale. Increasing the height of the magma system would increase the transient overturn timescale.

[22] Figure 1 shows a typical simulation throughout a cycle of overturn. *Youngs* [1984] described the mixing process in the fully turbulent regime by three evolutionary stages. Although turbulent con-

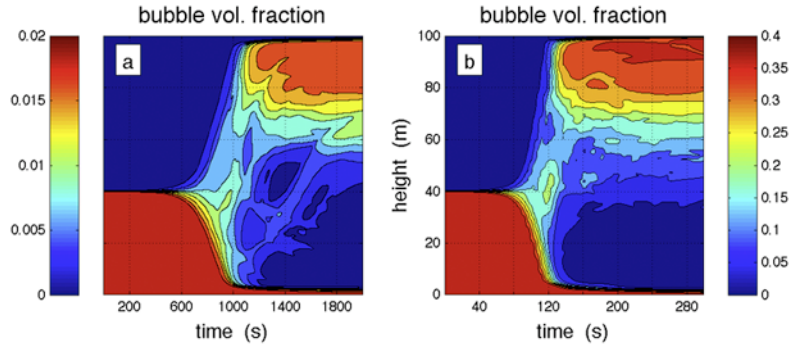

Figure 2. Horizontally averaged bubble volume fraction evolution as a function of time. The overturn is characterized by three stages: a buildup of the instability, the transient and chaotic upward transport of the bubble-bearing magma, and the damping of the overturning motion that creates a stratified magmatic system. (a) Low *Re* number case for bubble volume fraction of 0.02. The transient mixing dynamics occur on a timescale of 10^3 s. (b) High *Re* number case for bubble volume fraction of 0.4. The transient mixing dynamics occur on a timescale of 10^2 s. Note the different time axes for the two time series. Auxiliary material Animation 1 shows how Figure 2 is generated from Figure 1.

ditions are not likely to occur in silicic magmatic systems, the same growth stages could be recognized. A complete video of this simulation can be found in the electronic supplementary data. Initially, the instability grows exponentially until the characteristic wavelength λ_m emerges. Results for predicted λ_m ranging from 39.2 m and 77.9 m (Table 2) are in good agreement with our initial condition requiring the generation of multiple plumes in the 200 m wide system. Observed wavelengths are of similar order. This length scale dominates the second evolutionary stage, in which those plumes rise undisturbed to about $\lambda_m/2$. Subsequently, the plume head grows in width by entrainment and the associated vortical circulation influences the neighboring plumes causing their internal structure to become increasingly more complex. In addition, local Kelvin-Helmholtz instabilities develop along the interface of the rising plume. These instabilities generate eddies between the upward moving lighter melt-bubble mixture and the downward moving magma. All these interactions temporally and spatially cause stretching and translation.

[23] Once the bubble-rich plumes reach the top, they spread out and create a layer of bubble-rich magma. While the main plumes move upward through the system, a second wave of smaller plumes with a range of length scales emerges from the remaining bottom layer. Plume generation continues until the initial bubble-rich layer at the bottom is consumed. Similar behavior was described by *Bergantz and Ni* [1999].

[24] The process of convective overturn creates a gradually stratified magma chamber overlying bubble free magma. The first wave of plumes produces the largest eddies and is most efficient in mixing in magma of the overlying bubble-free layer. They entrain and deform large volumes of the overlying magma that get stretched and redistributed by subsequent smaller plumes. This stirring associated with stretching and redistribution leads to local homogeneity in the progress toward a gradual vertical stratification. Finally, this gradual stratified layer becomes increasingly concentrated in bubbles at the top, while the bubbles continue to rise separately or in small bubble trains. We do not observe an increase in bubble volume fraction within the top layer beyond its initial volume fraction. As mention earlier, our model ignores bubble coalescence, which results in a maximum rise speed of the bubbles equal to the terminal rise velocity of $10^{-1}\mu$m/s for the 1 mm large bubbles. This limits the vertical accumulation of bubbles over the short timescale of this transient overturn.

[25] Figure 2 represents the temporal evolution shown in Figure 1 in a more compact form. One can recognize the temporal evolution from instability growth, the subsequent dynamic mixing by overturn, to the final stratification. The two end-member simulations are shown in Figure 2. In the small *Re* case ($\varepsilon_{bubbles}$ = 0.02) multiple pulses of plume generation are shown within the time series of horizontally averaged $\varepsilon_{bubbles}$. In the high *Re* case ($\varepsilon_{bubbles}$ = 0.4) several plume generation events are also present, but occur at a higher

frequency and are therefore not as well defined by the horizontal averaging used in Figure 2. Additionally, for small bulk *Re* numbers (i.e., small bubble volume fractions) the zone of stratification is smaller than for large *Re* numbers (Figure 2). In the high *Re* case more of the bubble free magma is dragged into the vortices of the plumes, thus more efficiently mixed into the bubbles-bearing magma. *Bergantz and Ni* [1999] presented similar results on the sedimentation of dripping crystal-bearing plumes in viscous fluids. It was confirmed that for high-viscosity fluids (low *Re*) the mixing efficiency was much smaller than for low-viscosity fluids (high *Re*).

[26] The overturning process produces mixing of the bubble-free and the bubble-bearing layers. Several approaches have been used to quantify the efficiency of the mixing, such as various statistical measures of the progressive change of the concentration field during the mixing process [*Oldenburg et al.*, 1989], changes in the interface length [*Ottino*, 1990] and the change in potential energy of the system [*Linden and Redondo*, 1991]. We adopt a slightly modified version of this latter approach [*Jellinek et al.*, 1999]. The mixing efficiency, *E,* is an expression for the vertical stratification, or gradient, of a mixed quantity at the end of overturn [*Linden and Redondo*, 1991]:

$$E = \frac{(P_f - P_{\min})}{(P_{\max} - P_{\min})}, \tag{13}$$

$$P_f = \int_0^H g(\rho_{melt} - \rho(z))z dz, \tag{14}$$

where P_f is the integrated potential energy of the stratified system. $P_{\min}$ and $P_{\max}$ correspond to no mixing where the two layers exchange position without mixing, and complete mixing, where the mixture composition is the same everywhere. Mixing efficiency is generally low for this fixed volume system, resulting in a stratified system. The simulation with the highest bubble volume fraction reaches a mixing efficiency of 0.45. Low mixing efficiencies for the magmas imply an equally low mixing efficiency for crystals that are dispersed in the flow, since for a fast overturn process and small crystal diameters, crystals will have a Stokes number [*Burgisser et al.*, 2005] much less than unity and so simply follow the flow. However, since there is some mixing present, it is of interest on which length scales the crystal gathering and dispersal is observed.

4. Linking the Dynamics of Crystal Gathering and Dispersal to Geological Observations

[27] Crystal gathering and dispersal is a function of the strain associated with the redistribution and stretching during the mixing process [*Kellogg and Turcotte*, 1990]. During strain accumulation for a 2-dimensional system a circle with radius a_0 is deformed into an ellipse with a long and a short axis of length a_i, where i refers to the two perpendicular directions. Similarly to a circle, we can compare the distance between two points that are initially separated by the distance a_0. In mantle mixing studies [*Kellogg and Turcotte*, 1990; *Ferrachat and Ricard*, 1998; *Coltice and Schmalzl*, 2006] the change of a_i with respect to a_0 for these two points has been used to investigate the mantle flow dynamics. The change of a_i is commonly expressed as the Lyapunov exponent σ_i:

$$\sigma_i = \lim_{\substack{t\to\infty \\ a_0\to 0}} \frac{1}{t} \ln\left(\frac{a_i}{a_0}\right). \tag{15}$$

A system is chaotic and mixing is efficient on the local scale if one Lyapunov exponent is positive [*Ferrachat and Ricard*, 1998]. In contrast, Lyapunov exponents equal to zero indicate regular mixing.

[28] The tracked crystals in the simulations are tracers of individual particles and act owing to their low Stokes numbers simultaneously as tracers of small volumes of magma. Thus, we can use the advected crystals to estimate the strain a_i/a_0 and the Lyapunov exponent by choosing particle pairs for which a_0 is sufficiently small. By calculating the distance a_0 between all $\sim 2.0 \times 10^8$ crystal-crystal pairs ($(n(n-1))/2$ for $n = 20{,}000$ crystals) for their initial location, we can select those crystal-crystal pairs that are closer to each other than an arbitrarily chosen cutoff distance. We call this cutoff distance the Maximum Crystal-Crystal Distance (MCCD) (Figure 3). Following equation (15) the MCCD needs to be as small as possible to determine σ for the local scale. Hence, the limiting factor is statistical significance for the number of pairs that fall within this distance.

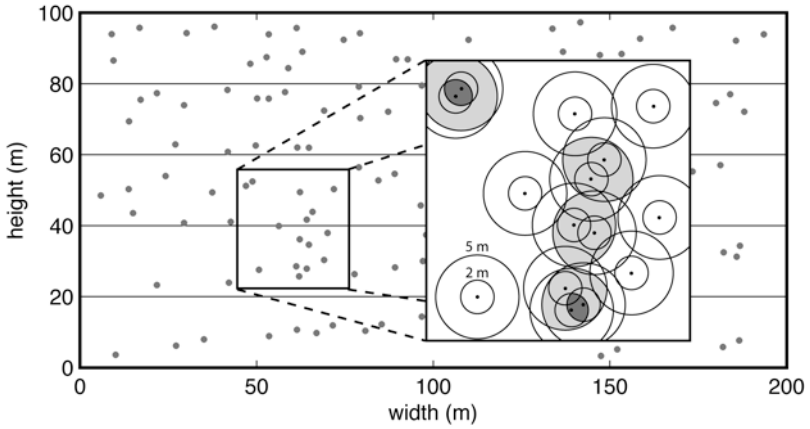

Figure 3. Technique for investigating crystal dispersal and gathering. For each "smart crystal" the distance to all other crystals was calculated and only crystal pairs closer to each other than the Maximum Crystal-Crystal Distance (MCCD) were chosen for the prior-after overturn comparison. The inset represents a subset of crystal locations after the overturn. The circles around each crystal represent the 2 m and 5 m MCCD, respectively. In this example, the particle pairs falling in the dark gray and light gray areas are chosen for a comparison of their location prior to and after the overturn for the 2 m and 5 m case. Thus, only a subset of the $n(n-1)/2$ crystal pairs are used for the analysis. We select those pairs for the entire volume as well as 20 m thick layers.

[29] The selection criterion for the statistical analysis of a crystal-crystal pair therefore is

$$a_0 \leq MCCD. \tag{16}$$

[30] Figure 4 shows the time series of the Lyapunov exponent for the simulations with varying bubble-volume fraction and for a MCCD of 2 m. For the gas-driven overturn with variable bubble-volume fraction the Lyapunov exponents are positive, but several orders of magnitude smaller than σ for mantle mixing studies [*Coltice and Schmalzl*, 2006], which may be as high as 10^5. Values for σ in Figure 4 are only minimum estimates, because our calculations ignore the possibility of folding. The vorticity that the crystal pair experiences needs to be considered for an exact calculation of the maximum Lyapunov exponent [*Wolf et al.*, 1985]. We ignore this effect, because the tracking of folding is computationally expensive and because we argue below that a modified version of the Lyapunov exponent is a better measure to characterize the mixing dynamics of gas-driven overturn.

[31] On the basis of the estimates for *Re* we know that gas-driven overturn is chaotic for the presented range in bubble-volume fractions. However, Figure 4 shows that σ_{max} asymptotically approaches zero with time, which indicates regular mixing. This disagreement stems from the fact that transient flows have a finite strain a_i/a_0. Once the potential energy of the initial instability is dissipated a_i remains constant, thus σ_i intrinsically has to approach zero asymptotically. Even so, the calculated *Re* at peak strain rates yields a chaotic mixing regime. While for statistically steady but time-dependent flows, as observed in mantle dynamics, a Lyapunov exponent can be calculated following equation (15), transient flows, which dominate crustal magma processes, cannot be characterized very well with the conventional Lyapunov exponent. Therefore, we favor estimating the strain over the use of the Lyapunov exponent in

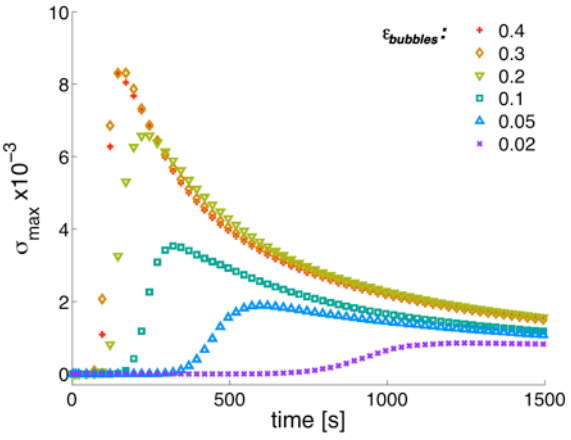

Figure 4. Time series for the maximum Lyapunov exponent σ for $a_0 = 2$ m. A positive σ indicates chaotic mixing during the transient gas-driven overturn. Once that transient signal decays, σ also asymptotically approaches zero. For further discussion, see text.

the gas-driven overturn to characterize the dynamic behavior.

[32] The strain for adjacent particles enables us to connect the process of gas-driven overturn directly to petrologic observations. Petrological analysis is typically based on small-sized samples, and one objective is to understand how compositional and textural heterogeneity at that scale reflects a distinct set of dynamic processes at much larger scales. Thus, one must resolve crystal paths through all scales of the flow. By comparing adjacent crystals on the basis of their spacing prior to the onset of a dynamic process such as mixing, and their final spacing after the process has finished, we can estimate the average dispersal and gathering for a given crystal-crystal pair, which is equal to the local strain. This in turn gives an estimate of the volume that is sampled in a single thin section during a single overturn. While commonly the strain is calculated on the basis of initially adjacent particles, we calculated the strain from crystal pairs that are close to each other AFTER the overturn event. Thus, we can use the simulations to understand natural examples, in which we can only image the final stage. As discussed in section 2, we define the end of the transient signal as the time when the average crystal motion has fallen below 0.08 mm s^{-1}. Therefore, the accumulated strain that we compare for the different simulations is defined as

$$strain = \frac{a_0}{a_{final}}, \tag{17}$$

$$a_{final} \leq MCCD. \tag{18}$$

Note the different selection criterion compared to equation (16) that is commonly used to calculate the Lyapunov exponent. This strain calculated from the crystal-crystal pairs is a measure for the gathering strength of the flow and compares the original volume that is tapped during the mixing. For a_0/a_{final} equal to one no differential movement between the crystals has occurred, while a value larger than one indicates gathering of the crystals from a larger volume.

[33] Ideally, the MCCD should be 3 cm, the scale of a thin section. However, given 20,000 randomly distributed tracer crystals over the entire system restricts this approach to larger MCCDs, to ensure statistical significance. A MCCD of 10 cm reduces the population size to $\sim 1 \times 10^4$ crystal-crystal pairs. We have chosen seven different MCCDs with 0.1 m, 0.2 m, 0.5 m, 1 m, 2 m, 5 m, and 10 m, respectively. The population size for the largest MCCD (10 m) increases to $\sim 6 \times 10^6$ crystal-crystal pairs.

[34] To evaluate crystal transport over the entire system, we plot the strain accumulation for all crystal-crystal pairs that meet the selection criterion for a specific simulation in a cumulative frequency distribution (CFD) (Figure 5). We choose the median of the CFD to be the measure of the average strain accumulation for all crystal-crystal pairs in that simulation. The larger the median of the CFD, the larger is the volume of crystal gathering. Additionally, we choose the slope, calculated between the first and third quartile of the CFD, as a measure for the homogeneity of the gathering for all particle-pairs. A large slope indicates a homogeneous behavior for the crystal-crystal pairs. In this case, different crystal-crystal pairs are gathered over a large and continuous range of length scales. In contrast, a large slope indicates that most crystal-crystal pairs are gathered from a volume with similar length-scale. Only a very minor proportion of crystal-crystal pairs is gathered either from a very small or from a very large length scales.

[35] To exemplify the process described above, we apply these concepts of strain accumulation and crystal-crystal pair homogeneity to four cases of our simulation runs, thus combining the information from the bulk multiphase model and the crystal-tracking algorithm (Figure 5). The runs with a bubble volume fraction of 0.1 and 0.3 correspond to the low and high *Re* numbers in our simulations, respectively. In Figure 5 we compare these runs for a small (0.1 m), and an intermediate (1 m) MCCD, respectively. Larger MCCDs have limited value for the connection of modeling data with thin section scale observations. In all four cases over 95% of the crystal-crystal pairs have a a_0/a_{final} greater than one. For the average particle (median) this gathering range varies over one log unit from $10^{1.5}$ to $10^{2.5}$ of their final distance. Thus, most crystals with a $a_{final} \leq$ MCCD are between 30 to 300 times further apart of each other before the mixing.

[36] Comparing the CFDs in Figure 5 for the low and the high *Re* case in more detail reveals a weaker strain accumulation for low *Re*. This behavior is observed for large and small MCCDs. The difference in the median of the CFD between high and low *Re* case for both MCCDs is $\sim$0.15 log units, respectively. Additionally, the strain

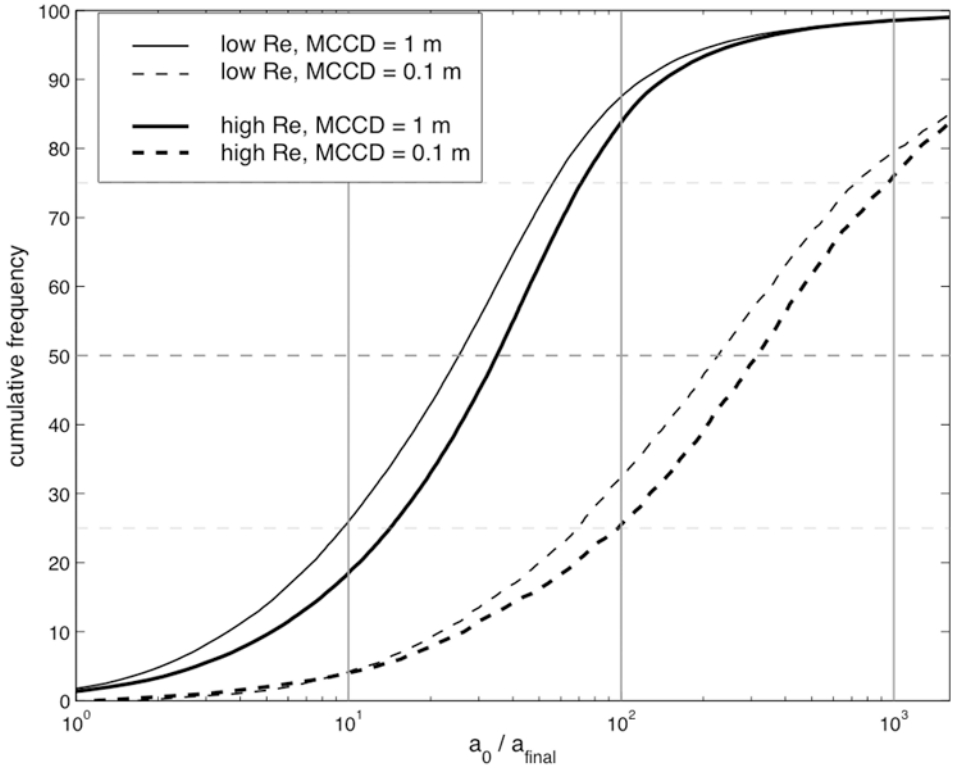

Figure 5. Cumulative Frequency Distribution (CFD) curves for populations of particle pairs within threshold proximity after the mixing event. High and low Re cases refer to $\varepsilon_{bubbles}$ = 0.3 and $\varepsilon_{bubbles}$ = 0.01, respectively.

accumulation increases, for a smaller MCCD. Besides the shift to larger medians for small MCCDs, we also observe a decrease in the slope of the CFDs. For small MCCD the distribution gets very broad, indicating that the crystals experience very different gathering length scales. The largest heterogeneity in gathering length scales occurs for low *Re* and small MCCD.

[37] We have also analyzed these crystal-crystal pairs of the two different simulations ($\varepsilon_{bubbles}$ = 0.1; $\varepsilon_{bubbles}$ = 0.3) for varying horizontal behavior of particles for the smallest MCCD (0.1 m) case (Figure 6). The crystal-crystal pairs are divided into five horizontal layers of 20 m each. Not all layers are shown; instead Figure 6 shows an envelope that is composed of the CFDs of all five horizontal layers. As expected, the range of gathering displayed by this envelope varies around the average value for the entire crystal population. For the low *Re* case this range is much larger (~0.6 log units) than the range observed in the high *Re* case (~0.2 log units). This discrepancy stems mainly from the initially bottom layer in the low *Re* case, which shows a significantly smaller length scale in gathering. Thus, while the kinematic behavior for the uppermost 80 m is very uniform with fairly small scatter around the average value, the lowermost bubble-bearing magma shows a different kinematic behavior. The lowermost 20 m stay more coherent over the course of the overturn then the rest of the magma and are less vigorously mixed.

[38] While the results for 20,000 randomly distributed "smart" crystals show an unambiguous trend of heterogeneous behavior on the bulk and the crystal scale, they were only applied to two of the six simulated $\varepsilon_{bubbles}$. The remaining simulations with different $\varepsilon_{bubbles}$ are also analyzed for the relative crystal-crystal pair motion. However, we have reduced the number of tracked crystals to n = 5000, hence minimizing computational time.

[39] These simulations decrease the number of crystal-crystal pairs that can be analyzed by a factor of $\sim 1/4^2$ ($(n(n-1))/2 = 1.25 \times 10^7$). This requires an increase in the MCCD to the meter scale. In fact, for an MCCD of 1 m we generate only $\sim 3 \times 10^3$ crystal-crystal pairs for the statistical analysis. For an MCCD of 10 m we have more than one order of magnitude less crystal-crystal pairs available ($\sim 4 \times 10^5$) compared to the simu-

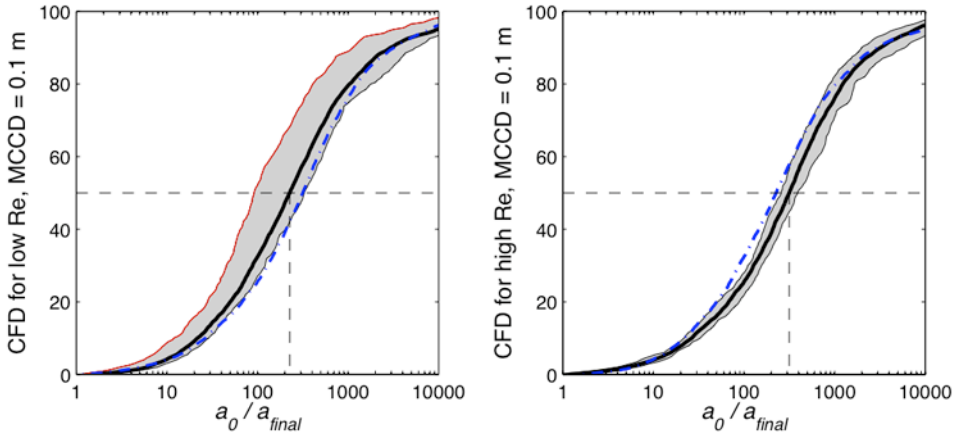

Figure 6. Cumulative Frequency Distribution (CFD) curves for high-resolution simulations with 20,000 "smart" particles. The low Re case ($\varepsilon_{bubbles}$ = 0.10) on the left is compared with the high Re case ($\varepsilon_{bubbles}$ = 0.30) on the right. The black line represents the CFD for the entire population; the blue dashed line is the opposite case for comparison. The gray field outlines the variability of CFDs for different horizontal regions in the simulation. The low Re case is composed of much more variability; in particular, the lowermost layer (red outline) shows smaller amounts of strain accumulation.

lations with 20,000 crystals. Thus, for these lower resolution simulations we do not reach a length scale that is similar to the length scale of a thin section. However, in light of the high-resolution simulations with 20,000 "smart" crystals, these additional simulations expand our understanding for the simulations with the lowest and highest *Re* numbers, respectively.

[40] Instead of presenting the results from the additional simulations with 5000 "smart" crystals in separate cumulative frequency diagrams, we summarize all simulations by their strain accumulation and their particle population homogeneity (Figure 7). At high *Re* mixing events are characterized by smaller particle population heterogeneity and stronger strain accumulation. Comparing the large MCCD (10 m) with the small MCCD (0.1 m) of crystal gathering as a function of changing *Re* number reveals a shift from small variations in strain accumulation and large changes in particle population homogeneity to mainly strain accumulation dominated behavior. The simulations with 5000 "smart" crystals follow the trend of the high-resolution simulations. They also support that simulations with large $\varepsilon_{bubbles}$ (0.2, 0.3, and 0.4) are very similar to each other. This is in good agreement with the observed *Re* numbers (Table 2) that identify a very similar mixing behavior on the bulk scale. The simulations with low $\varepsilon_{bubbles}$ are more variable in their strain accumulation and particle population homogeneity.

[41] Figure 7 also enables us to assess the statistical robustness for the small MCCD cases. The results from the high-resolution simulations with 20,000 "smart" crystals have very similar values for the strain accumulation and the particle population homogeneity as the simulations with 5000 "smart" crystals. The smallest chosen MCCD (1 m) for the smaller number of "smart" crystals starts to diverge from the results of the high-resolution simulations. Thus, any smaller MCCD would not be statistically robust.

5. Discussion

5.1. Length Scale of Crystal Gathering in Thin Section

[42] The results from the coupled multiphase-particle tracking simulations show that in a single overturn, most crystals that end up in the same small-scale volume are gathered over tens of meters during one overturn. A significant proportion (~20%) of the crystal cargo may have originated from a distance of 100 m or more from each other. Therefore, a single mixing event is capable of juxtaposing crystals that originated from spatially distinct regions of the chamber, and with completely different histories (compositional zoning, textures, etc.). Thus, heterogeneous populations with chemical variations and kinked crystal size distributions are common [*Morgan et al.*, 2007].

[43] Our methodology is also applicable to a closed-system, in which heat transfer occurs through the walls. *Singer et al.* [1995] employed the dynamic template of quasi-steady overturn as

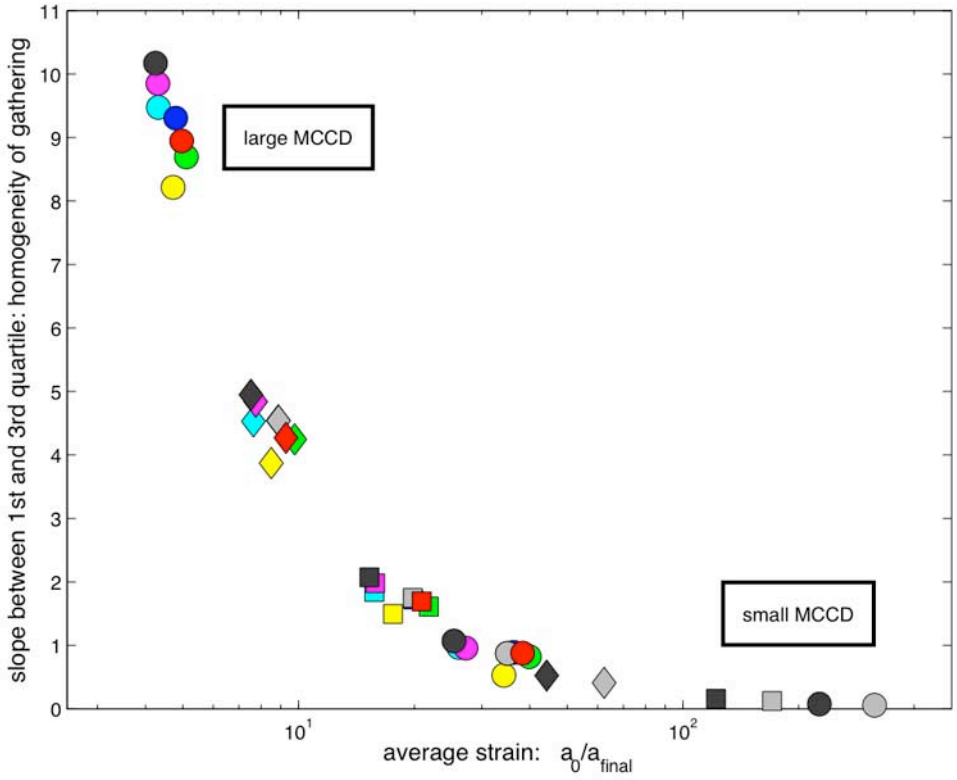

Figure 7. All population CFDs are represented with their median and a slope calculated using the first and third quartile. $\varepsilon_{bubbles}$: 0.02 (yellow), 0.05 (cyan), 0.10 (magenta), 0.20 (green), 0.30 (blue), 0.40 (red). MCCD: 10 m (circles), 5 m (diamonds), 2 m (squares), 1 m (circles), 0.5 m (diamonds), 0.2 m (squares), 0.1 m (circles). Gray symbols are runs with 20,000 particles, where $\varepsilon_{bubbles}$: 0.10 (dark), 0.30 (light). All other CFDs were calculated for 5000 "smart" particles.

proposed by *Marsh* [1988, 1989]. Our simulations with the lowest bubble-volume fraction might be an appropriate proxy for this case. For $\varepsilon_{bubbles}$ of 0.05 and 0.10, density differences between the two layers are 3.7% and 7.5%, respectively. The dynamic viscosity varies by 0.7% and 3.2%, respectively (Table 2). These are reasonable for the sluggish closed-system processes. Even at these low bubble volume fractions, chaotic mixing dominates and we expect the crystal cargo to be heterogeneous. This chaotic behavior limits the extent of repeated zoning patterns in crystals experiencing cyclical magma overturn in a closed system.

5.2. Damköhler Numbers for Crystal Growth and Dissolution

[44] Crystals that are transferred to a different chemical environment by convective motion may react to those changes in chemical potential by dissolution or crystallization. However, the record of this transport may be incompletely preserved in the crystals. How much of this data is recorded is a competition between the reaction and transport timescales. For example, at the fastest transport rates, during the ascent in a conduit, it has been shown that the crystal recorder is too slow to record the transient changes [*Kerr*, 1995]. To understand fully the interplay between crystal response time and transport time requires a kinetic model for crystal nucleation, crystal growth and/or resorption. Our knowledge of nucleation, crystallization and resorption under magmatic conditions is limited [*Hersum and Marsh*, 2007]. Several authors [*Dowty*, 1980; *Cashman*, 1990; *Larsen*, 2005] have compiled existing experimental data on nucleation and growth kinetics and data on crystal growth inferred from crystal zoning studies. These compilations include results from simple binary systems, e.g., growth kinetics in the system of albite-anorthite solid solution, as well as from multicomponent systems resembling closer natural magma compositions. *Larsen* [2005] reports a range for crystal growth rates G from 10^{-1} mm s^{-1} to 10^{-11} mm s^{-1}. The largest growth rates have

only been observed in very simplified systems. Therefore, we focus furthermore on the growth rates G for multicomponent compositions that range from 10^{-6} mm s^{-1} to 10^{-11} mm s^{-1}.

[45] Recent results from decompression experiments on the 1991 Pinatubo dacite [*Hammer and Rutherford*, 2002], on a synthetic composition of the 1996 andesitic Montserrat dome [*Couch et al.*, 2003], and on a synthetic haplogranitic composition [*Couch*, 2003] suggest maximum plagioclase growth rates G on the order of 10^{-6} mm s^{-1}. Crystallization decompression-induced degassing is viewed as one of the fastest crystallization mechanisms. Therefore, these growth rates constitute a lower time limit on noticeable plagioclase growth.

[46] The competition between the reaction timescale t_{react}, i.e., crystallization or dissolution, and the transport timescale t_{ad}, i.e., advection, can be compared by defining a Damköhler number Da,

$$Da = \frac{t_{ad}}{t_{react}}, \tag{19a}$$

$$Da = \frac{t_{overturn}}{t_{react}}, \tag{19b}$$

$$t_{ad} = \left(\frac{H}{gA}\right)^{1/2}, \tag{20}$$

$$t_{overturn} = \text{timescale obtained from multiphase simulations}, \tag{21}$$

$$t_{react} = \frac{d}{G}, \tag{22}$$

where t_{ad} is the theoretically derived advection timescale by *Linden and Redondo* [1991] and $t_{overturn}$ is the numerically derived advection timescale obtained from the overall duration of each of our simulations (Table 2). This timescale $t_{overturn}$ is the total time of instability growth, overturn and damping after the overturn has ceased. The theoretical advection timescale t_{ad} is a measure for the time it takes for the mixing region to extend throughout the fluid. The reaction timescale t_{react} is estimated by the growth rate G and a resolvable length scale d of crystal overgrowth (d = 1 μm) using an electron microprobe [*Ginibre et al.*, 2002]. For $Da \ll 1$ the advective transport is much faster than significant crystal growth.

[47] On the basis of the growth rate G in natural systems and the theoretically derived advection timescale t_{ad} we calculate $Da \ll 1$ (Figure 8a). The Da number ranges over one order of magnitude for a given crystal growth rate. The lowest estimates of crystal growth rates ($G = 10^{-11}$ mm s^{-1}) that are inferred from crystal zoning studies result in $Da < 10^{-6}$. Decompression and degassing-induced crystallization as assumed for our multiphase simulations shows $Da < 10^{-1}$. Even for the most sluggish case with the largest advection timescale and the fastest growth rates we find the $t_{ad} \ll t_{react}$ ($Da \approx 0.04$).

[48] Considering $t_{overturn}$ as advection timescale causes Da numbers to be significantly larger (Figure 8b). Let us only focus on the case for crystal growth rates induced from decompression experiments ($G = 10^{-6}$ mm s^{-1}), since these conditions are most reflective of our multiphase simulations for gas-driven overturn. If we choose $t_{overturn}$ as defined earlier, the time until average crystal motions has slowed down to 0.08 mm s^{-1}, we consistently observe $Da > 1$. However, this advection timescale is a maximum timescale by including the initial growth of the instability, the transient overturn, and the final waning of the mixing process. A better measure for the advection timescale is the transient overturn itself, since this is the time when extreme variations in chemical potential exist. The duration of the transient stage of the overturn is on the order of 10^2 to 10^3 s (Figure 2). This advection timescale is still more than one order of magnitude larger than t_{ad} obtained from linear theory. The resulting Da number ranges from 10^{-1} to 1 for large and small $\varepsilon_{bubbles}$, respectively. Thus, under this assumption the advection and the reaction timescale are of similar order for small density differences (i.e., $A \approx 0$) between the bubble-free and the bubble-bearing magma.

[49] In summary, we find that for magma overturn due to large density differences (i.e., $\varepsilon_{bubbles} \geq 0.2$) existing crystals record only their initial and final disequilibrium environment. They may not record the short-lived extremes in intensive variables that drive mixing or overturn. Once the transient overturn has ceased, bubbles and crystal may settle to their neutral buoyancy level. During the settling crystals may record the change in chemical potential associated with the observed stratification. For a natural system, in which bubble-rich andesite recharge mixes with a more evolved magma, crystals would potentially be normally zoned.

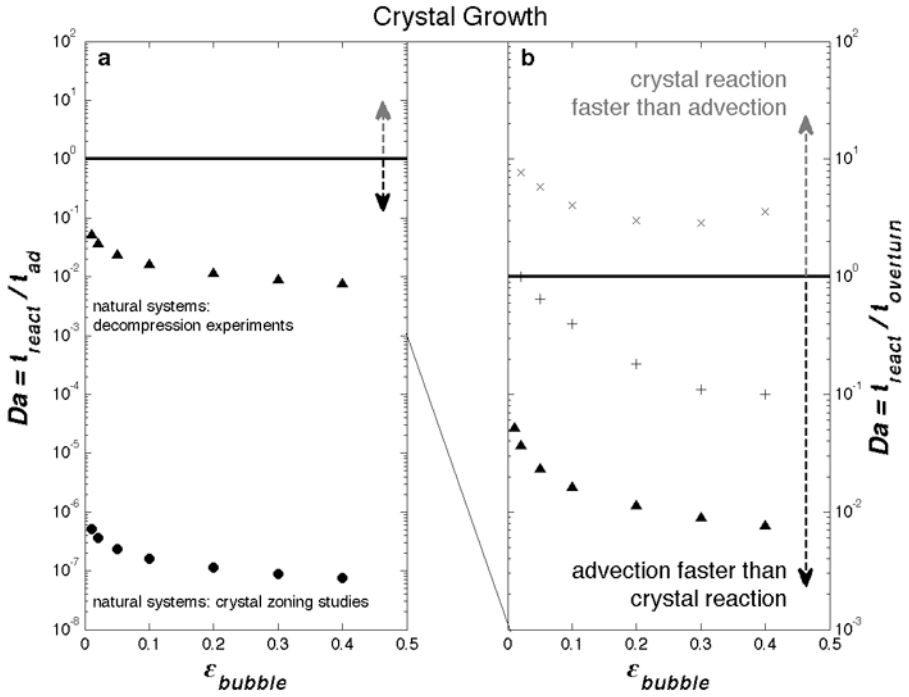

Figure 8. Damköhler number *Da* for crystal growth plotted versus bubble volume fraction ($\varepsilon_{bubbles}$). For $Da \ll 1$ advection is faster than crystal growth. (a) *Da* numbers using the theoretical advection timescale after *Linden and Redondo* [1991] compared to two different growth rates *G* of 10^{-6} mm s^{-1}(Δ) and 10^{-11} mm s^{-1}(O), respectively. (b) *Da* numbers for the numerically derived advection timescale and reaction timescale from decompression experiments. The advection timescale presented in Table 2 (X) combines the initiation of the instability, the overturn, and the damping after overturn until average crystal movement has decreased below 0.08 mm s^{-1}. Considering only the transient overturn (+) reduces the *Da* numbers by an order of magnitude. (Δ) as in Figure 8a.

[50] For very sluggish system with small density differences crystal growth and magma mixing are of similar order of magnitude. In this case crystal growth is not negligible during the overturning process.

[51] In contrast to crystal growth, crystal dissolution may, even for large $\varepsilon_{bubbles}$, more faithfully keep pace during the transient part of the gas-driven overturn (Figure 9). Dissolution rates G_{Dis} for natural melt compositions based on experimental data [*Donaldson*, 1985; *Zhang et al.*, 1989] and dissolution models [*Liang*, 2000, 2003] are on the order of 10^{-4} to 10^{-6} mm s^{-1}. Thus, analogous to the discussion about crystal growth during gas-driven overturn we calculate $Da \geq 1$.

[52] The effects on the *Da* number caused by processes that may slow down the dissolution process can only be discussed qualitatively. Parameters that influence the dissolution rate are the dissolution mechanism, melt viscosity and melt composition [*Shaw*, 2006]. In particular, the dissolution mechanism, which is a competition between interface-controlled and diffusion-controlled dissolution, has strong effects on the dissolution kinetics. While interface-controlled growth may complicate the dissolution kinetics [*Shaw*, 2006], it has been reported that for highly viscous melts dissolution is generally diffusion-controlled [*Jackson and Mills*, 1997]. Therefore, we will focus our discussion on diffusion-controlled dissolution. A complete discussion on dissolution rates and dissolution mechanisms can be found in the review by *Edwards and Russell* [1996] as well as in the paper by *Shaw* [2006].

[53] Diffusion-controlled dissolution results in a time-dependent dissolution rate [*Zhang et al.*, 1989] and the progress of a dissolution front d_{dis} can be estimated by [*Liang*, 2000, 2003]:

$$d_{dis} = 2\alpha(D_1 t)^{1/2}, \tag{23}$$

where α and D_1 are the dimensionless diffusion parameter and the diffusion coefficient of component 1 in the liquid, respectively. Dissolution calculations are generally performed for α =

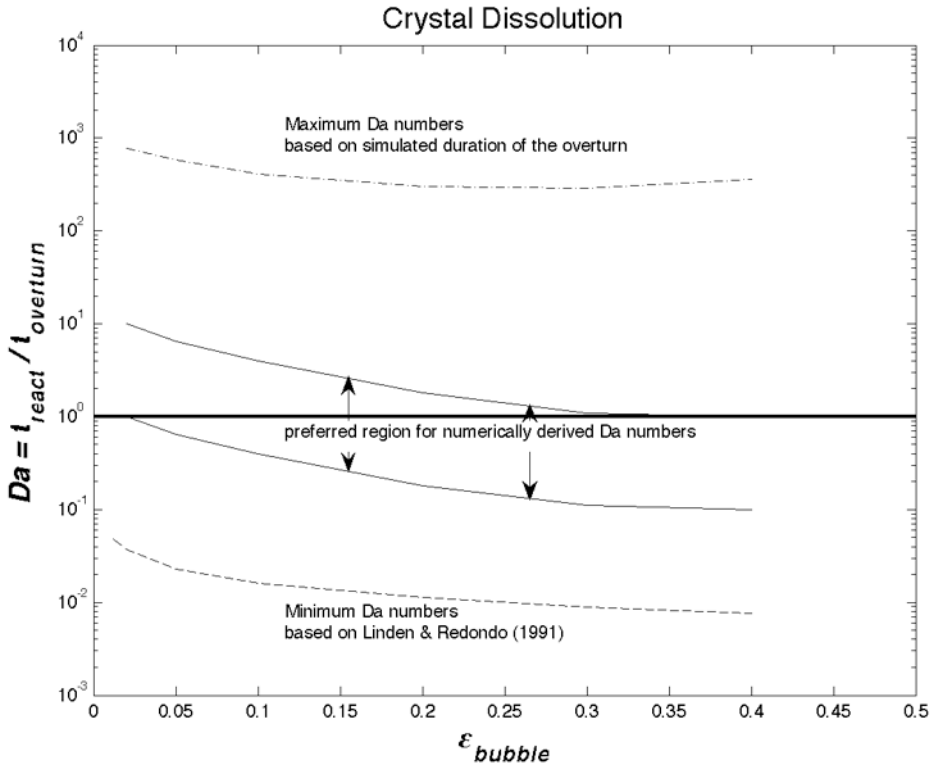

Figure 9. Damköhler number *Da* for crystal dissolution plotted versus bubble volume fraction ($\varepsilon_{bubbles}$). For $Da > 1$, crystal dissolution is taking place during magmatic overturn. The preferred region of *Da* numbers (solid lines) is ≈1 for all $\varepsilon_{bubbles}$, indicating a tight competition between dissolution and advection. It is calculated for advection timescale obtained from the transient overturn stage and dissolution rates G_{Dis} from 10^{-5} mm s^{-1} to 10^{-6} mm s^{-1}. Minimum estimates (dashed lines) for *Da* are based on slow dissolution rates (10^{-6} mm s^{-1}) and as well as t_{ad}. Maximum estimates (dashed-dotted lines) for *Da* are calculated for the fastest dissolution (10^{-4} mm s^{-1}) and the overturn timescale from Table 2.

−0.4 [*Liang*, 2003] and D_1 between 10^{-11} m^2 s^{-1} and 10^{-14} m^2 s^{-1} (D_1 taken from *Watson* [1994]).

[54] A more detailed examination of the diffusion processes [*Zhang et al.*, 1989, *Liang*, 2003] shows that the dominating dissolution rates are close to the lower limit (G_{Dis} = 10^{-6} mm s^{-1}) of the reported range. The dissolution rate limiting parameters are the diffusion coefficient for the components of the crystal and the nonlinear behavior of equation (23) ($d_{dis} \sim t^{1/2}$). Following *Liang* [2003] the dissolution process is limited by the slowest diffusing component in a multicomponent system, thus small diffusion coefficients (D_1 = 10^{-14} m^2 s^{-1}) have the largest impact on the dissolution kinetics. Additionally, considering the dissolution rate over time we observe the highest dissolution rates only in the first few seconds of dissolution. This short time interval is insufficient to significantly dissolve the crystal. Within 10^2 s the overall dissolution rate falls off by a factor of $10^{1.5}$. Thus, the effective dissolution rate for processes on the order of 10^2 s to 10^3 s, which we investigate in our multiphase simulations, is probably on the order of 10^{-5} mm s^{-1} to 10^{-6} mm s^{-1} and $Da \approx 1$ (Figure 9).

[55] These results for the *Da* number indicate that crystal resorption will be limited to the crystal edges; anhedral to subhedral crystal textures will dominate the crystal cargo. These results are in good agreement with results on convective crystal dissolution by *Kerr* [1995] for convective motion in a magmatic dyke. Complete dissolution of crystals is unlikely. Instead, partial dissolution will occur because of the similar order of magnitude for advection and dissolution.

5.3. Crystallization and Dissolution During Temperature-Driven Convection

[56] While gas-driven convection is characterized by a tight competition between advection and

crystal reaction rates, advection timescales for temperature-driven convection are much slower. This causes crystal reaction rates to be orders of magnitude faster than advection rates. Our model for gas-driven convection assumes an instantaneous density inversion, which causes fast convection even for small $\varepsilon_{bubbles}$ and Da close to 1. Temperature-driven convection typically assumes a Rayleigh-Bénard convection cell [*Marsh*, 1988]. There may be heating from below due to underplating magma, but generally the magma system is governed by the conductive cooling through the roof and the sidewalls.

[57] Adopting the dynamic template of *Marsh* [1988] for temperature-driven convection results in large Da numbers between 10^1 and 10^6. An advective timescale t_{ad} of several years can be estimated for this dynamic template using equation (18) of *Marsh* [1988]:

$$U = \frac{K}{H} Nu^2, \tag{24}$$

$$t_{ad} = \frac{H}{U}, \tag{25}$$

where U, K, and Nu are the velocity, thermal diffusivity and the Nusselt number, respectively (For common rock material: $K = 10^{-6}$ m^2 s^{-1}). The Nusselt number relates the total heat transfer Q_{total} through the roof and the sidewalls to the heat transfer for conduction Q_{cond} alone:

$$Nu = \frac{Q_{total}}{Q_{cond}}. \tag{26}$$

Following *Marsh* [1988] we assume a maximum $Nu = 2$, since the roof and sidewalls may be insulated by a solidification front that grows inward toward the center of the magma chamber. The reaction timescale is the same as in equation (22) and varies for the range of observed growth rates in natural systems. As previously noted the fastest growth rates are typically observed in decompression experiments [*Hammer and Rutherford*, 2002; *Couch et al.*, 2003].

[58] Thus, the sluggish overturn due to temperature gradients is accompanied by slow growth rates between 10^{-8} mm s^{-1} and 10^{-11} mm s^{-1} [*Singer et al.*, 1995; *Davidson and Tepley*, 1997]. The slow removal of heat through the walls may reduce the effective undercooling that drives crystallization and subsequently crystallization itself is slowed down as well. Nonetheless, even for these slow growth rates we observe $Da \gg 1$. Thus, crystallization kinetics is fast enough to record various chemical conditions that may persist in the sluggish behaving magma chamber.

[59] While there is sufficient time for the crystal to record changes in chemical potential during purely temperature-related effects, there is also potentially enough time for complete crystal dissolution. Following the diffusion-controlled dissolution model of equation (23) we estimate a complete dissolution within days for millimeter-sized crystals. This would suggest that temperature-driven convection could completely erase the crystal record. However, to answer ultimately the question if dissolution is complete under such conditions we have to consider the simultaneous change in chemical potential. Extensive phenocryst dissolution will drive the system quickly to smaller degrees of undersaturation. Therefore, we expect that not the complete crystal is dissolved. Instead, small anhedral crystals may survive and record a strong dissolution surface between the remaining core and a significantly different newly growing mantle or rim as seen typically in arc magmas [e.g., *Ruprecht and Wörner*, 2007].

[60] Eruption triggering recharge events may subsequently gather chemically distinct crystal populations and without extensive modification of the crystal cargo transport this crystal assemblage to the surface [*Spera*, 1984; *Trial et al.*, 1992].

6. Conclusion

[61] Crystal-chemical and textural data from igneous systems reveal complex open-system behavior and internal circulation [e.g., *Singer et al.*, 1995; *Zellmer et al.*, 2003; *Ginibre et al.*, 2004]. Our results from a simple overturn model with viscosities applicable to intermediate and silicic systems [*Scaillet et al.*, 1998] show that this heterogeneity can even arise from a single overturning event. Multiple overturn events can lead to repeated gathering and dispersal of crystals and can obscure the apparent signature of crystals spatially residing together in a thin section (2.7 cm). Crystal-isotope-stratigraphy [*Davidson and Tepley*, 1997; *Davidson et al.*, 2007] has shown that arc magmas frequently gather crystals from isotopically very distinct environments. Gas-driven overturn is a very efficient process to facilitate the juxtaposition of crystal with distinct isotopic signature. On the basis of our calculations such a population of crystals is gathered over meters to tens of meters within a

single overturn. Therefore, the common path of a pair of crystals is probably very limited as has also been observed by *Wallace and Bergantz* [2005]. Systems with small density variations between the two mixing magmas have the largest potential for significant common path lengths between crystal-crystal pairs. However, even for those small *Re* cases we find this behavior only for a minor proportions of all crystal pairs.

[62] The common result from our multiphase mixing simulations (Figures 1 and 2) is not a homogeneous, but rather a stratified magma body with a maximum in $\varepsilon_{bubbles}$ on top and a continuous decrease in $\varepsilon_{bubbles}$ toward the bottom. Gradients are inevitable during a single overturn and mixing of the two instantaneously superimposed magmas is inefficient. This is due to the chaotic, not turbulent, flow regime for compositionally intermediate magmas. These heterogeneous environments of temperature and chemical gradients can persist over timescales much longer than the gathering timescale for gas-driven overturn, which is on the order of minutes to hours. These results are consistent with other fluid dynamic studies that predict final stratification in case of an instantaneous R-T instability [*Linden and Redondo*, 1991, *Jellinek et al.*, 1999]. We do not observe homogeneity neither on the bulk nor on the crystal scale. Crystals follow closely the fluid flow during gas-driven overturn. Therefore, the stratification in bubble-volume fraction after the overturn reflects also a stratification of crystal-origin. Crystals initially dispersed in the bubble-bearing magma are mixed into the bubble-free magma with similar proportions as is the bubble-bearing magma. A model that includes bubble coalescence may produce larger extents of differential movement between melt, crystals and bubbles of the recharging magma. However, the nonlinear processes of bubble coalescence, additional gas exsolution and secondary nucleation probably further increase the complex assembly of different crystal populations during the overturn.

[63] Considering the competition of crystal reaction rates with the advection rates during the overturn, we find that gas-driven advection is typically faster than crystal growth but of similar order in case of crystal dissolution. Thus, the crystals will not be able to record the actual mixing process with all its extremes in chemical potential. *Da* numbers less than 1 for crystal growth suggest that they will record only the stages prior-to, and following, the mixing event. In cases where dissolution is the response to the changes in chemical potential older stages of crystal growth may be erased. These conditions may vary from crystal to crystal and eventually may be sampled on the length scale of a thin section. Basically, any mixing will create a complex crystal population mixture even though the cause may be a simple low *Re* overturn. We investigated the most simplified system possible. Assuming mixing of chemically and/or physically different magma batches would constitute a much more complex initial condition. Such complex starting scenarios must inheritably increase even further complexity observed within the crystal population.

[64] For overturning processes that invoke longer timescales such as temperature-driven overturn the crystal cargo may record even more complex information, since crystallization rates, and therefore response through crystal growth to the changing environment may be faster than physical mixing rates [*Singer et al.*, 1995]. The resulting zonation record is likely to be more comprehensive and may include transient physical mixing processes.

Acknowledgments

[65] This work was supported by NSF grants EAR-0440391 and EAR-0711551 to G.W.B. and a Chevron Graduate Support Scholarship to P. R. We thank Jon Davidson and Yan Liang for very helpful and constructive comments on an earlier version of the manuscript.

References

Aref, H. (1990), Chaotic advection of fluid particles, *Philos. Trans. R. Soc. London, Ser. A*, *333*, 273–288, doi:10.1098/rsta.1990.0161.

Bachmann, O., M. A. Dungan, and P. W. Lipman (2002), The Fish Canyon magma body, San Juan volcanic field, Colorado: Rejuvenation and eruption of an upper-crustal batholith, *J. Petrol.*, *43*, 1469–1503, doi:10.1093/petrology/43.8.1469.

Beckermann, C., and R. Viskanta (1993), Mathematical modeling of transport phenomena during alloy solidification, *Appl. Mech. Rev.*, *46*, 1–27.

Bergantz, G. W., and R. E. Breidenthal (2001), Non-stationary entrainment and tunneling eruptions: A dynamic link between eruption processes and magma mixing, *Geophys. Res. Lett.*, *28*, 3075–3078, doi:10.1029/2001GL013304.

Bergantz, G. W., and J. Ni (1999), A numerical study of sedimentation by dripping instabilities in viscous fluids, *Int. J. Multiphase Flow*, *25*, 307–320, doi:10.1016/S0301-9322(98)00050-0.

Burgisser, A., G. W. Bergantz, and R. E. Breidenthal (2005), Addressing complexity in laboratory experiments: The scaling of dilute multiphase flows in magmatic systems*J. Volcanol. Geotherm. Res.*, *141*, 245–265, doi:10.1016/j.jvolgeores.2004.11.001.

Cashman, K. V. (1990), Textural constraints on the kinetics of crystallization of igneous rocks, in *Modern Methods of*

Igneous Petrology, Understanding Magmatic Processes, *Rev. Mineral.*, vol. 24, edited by J. Nicholls and J. K. Russell, pp. 259–314, Mineral. Soc. of Am., Washington, D. C.

Chandrasekhar, S. (1961), *Hydrodynamic and Hydromagnetic Stability*, 654 pp., Oxford Univ. Press, London.

Cioni, R., L. Civetta, P. Marianelli, N. Metrich, R. Santacroce, and A. Sbrana (1995), Compositional layering and syn-eruptive mixing of a periodically refilled shallow magma chamber: The AD 79 Plinian eruption of Vesuvius, *J. Petrol.*, *36*, 739–776.

Coltice, N., and J. Schmalzl (2006), Mixing times in the mantle of the early Earth derived from 2-D and 3-D numerical simulations of convection, *Geophys. Res. Lett.*, *33*, L23304, doi:10.1029/2006GL027707.

Coombs, M. L., and J. E. Gardner (2004), Reaction rim growth in silicic melts: Implications for magma mixing, *Am. Mineral.*, *89*, 748–759.

Couch, S. (2003), Experimental investigation of crystallization kinetics in a haplogranite system, *Am. Mineral.*, *88*, 1471–1485.

Couch, S., R. S. J. Sparks, and M. R. Carroll (2001), Mineral disequilibrium in lavas explained by convective self-mixing in open magma chambers, *Nature*, *411*, 1037–1039, doi:10.1038/35082540.

Couch, S., R. S. J. Sparks, and M. R. Carroll (2003), The kinetics of degassing-induced crystallization at Soufriere Hills Volcano, Montserrat, *J. Petrol.*, *44*, 1477–1502, doi:10.1093/petrology/44.8.1477.

Davidson, J. P., and F. J. Tepley, III (1997), Recharge in volcanic systems: Evidence from isotope profiles of phenocrysts, *Science*, *275*, 826–829, doi:10.1126/science.275.5301.826.

Davidson, J. P., D. J. Morgan, B. L. A. Charlier, R. Harlou, and J. Hora (2007), Tracing magmatic processes and timescales through mineral-scale isotopic data, *Annu. Rev. Earth Planet. Sci.*, *35*, 273–311, doi:10.1146/annurev.earth.35.031306.140211.

Derksen, J. J. (2003), Numerical simulation of solids suspension in a stirred tank, *AIChE J.*, *49*, 2700–2714, doi:10.1002/aic.690491104.

Donaldson, C. H. (1985), The rates of dissolution of olivine, plagioclase, and quartz in a basalt melt, *Mineral. Mag.*, *49*, 683–693, doi:10.1180/minmag.1985.049.354.07.

Dowty, E. (1980), Crystal growth and nucleation theory and the numerical simulation of igneous crystallization, in *Physics of Magmatic Processes*, edited by R. B. Hargraves, pp. 420–485, Princeton Univ. Press, Princeton, N. J.

Dufek, J., and G. W. Bergantz (2005), Transient two-dimensional dynamics in the upper conduit of a rhyolitic eruption: A comparison of closure models for the granular stress, *J. Volcanol. Geotherm. Res.*, *143*, 113–132, doi:10.1016/j.jvolgeores.2004.09.013.

Dufek, J., and G. W. Bergantz (2007), Dynamics and deposits generated by the Kos Plateau Tuff eruption: Controls of basal particle loss on pyroclastic flow transport, *Geochem. Geophys. Geosyst.*, *8*, Q12007, doi:10.1029/2007GC001741.

Edwards, B. R., and J. K. Russell (1996), A review and analysis of silicate mineral dissolution experiments in natural silicate melts, *Chem. Geol.*, *130*, 233–245, doi:10.1016/0009-2541(96)00025-3.

Eichelberger, J. C. (1980), Vesiculation of mafic magma during replenishment of silicic magma reservoirs, *Nature*, *288*, 446–450, doi:10.1038/288446a0.

Ferrachat, S., and Y. Ricard (1998), Regular vs. chaotic mantle mixing, *Earth Planet. Sci. Lett.*, *155*, 75–86, doi:10.1016/S0012-821X(97)00200-8.

Folch, A., and J. Martí (1998), The generation of overpressure in felsic magma chambers by replenishment, *Earth Planet. Sci. Lett.*, *163*, 301–314, doi:10.1016/S0012-821X(98)00196-4.

Gerlach, T. M., H. R. Westrich, and R. B. Symonds (1996), Preeruption vapor in magma of the climactic Mount Pinatubo eruption: Source of the giant stratospheric sulfur dioxide cloud, in *Fire and Mud: Eruptions and Lahars of Mount Pinatubo, Philippines*, edited by C. G. Newhall and R. S. Punongbayan, pp. 415–433, Washington Univ. Press, Seattle.

Gidaspow, D. (1994), *Multiphase Flow and Fluidization: Continuum and Kinetic Theory Descriptions*, 467 pp., Academic, Boston, Mass.

Ginibre, C., A. Kronz, and G. Wörner (2002), High-resolution quantitative imaging of plagioclase composition using accumulated backscattered electron images: New constraints on oscillatory zoning, *Contrib. Mineral. Petrol.*, *142*, 436–448.

Ginibre, C., G. Wörner, and A. Kronz (2004), Structure and dynamics of the Laacher See magma chamber (Eifel, Germany) from major and trace element zoning in Sanidine: A cathodoluminescence and electron microprobe study, *J. Petrol.*, *45*, 2197–2223, doi:10.1093/petrology/egh053.

Hammer, J., and M. J. Rutherford (2002), An experimental study of the kinetics of decompression-induced crystallization in silicic melt, *J. Geophys. Res.*, *107*(B1), 2021, doi:10.1029/2001JB000281.

Hersum, T., and B. Marsh (2007), Igneous textures: On the kinetics behind the words, *Elements*, *3*, 247–252, doi:10.2113/gselements.3.4.247.

Humphreys, M. C. S., J. D. Blundy, and R. S. J. Sparks (2006), Magma evolution and open-system processes at Shiveluch Volcano: Insights from phenocryst zoning, *J. Petrol.*, *47*, 2303–2334, doi:10.1093/petrology/egl045.

Jackson, M. J., and B. Mills (1997), Dissolution of quartz in vitrified ceramic materials, *J. Mater. Sci.*, *32*, 5295–5304, doi:10.1023/A:1018610710222.

Jellinek, A. M., and R. C. Kerr (1999), Mixing and compositional stratification produced by natural convection: 2. Applications to the differentiation of basaltic and silicic magma chambers and komatiite lava flows, *J. Geophys. Res.*, *104*, 7203–7218, doi:10.1029/1998JB900117.

Jellinek, A. M., R. C. Kerr, and R. W. Griffiths (1999), Mixing and compositional stratification produced by natural convection: 1. Experiments and their application to Earth's core and mantle, *J. Geophys. Res.*, *104*, 7183–7201, doi:10.1029/1998JB900116.

Kellogg, L. H., and D. L. Turcotte (1990), Mixing and the distribution of heterogeneities in a chaotically convecting mantle, *J. Geophys. Res.*, *95*, 421–432, doi:10.1029/JB095iB01p00421.

Kerr, R. C. (1995), Convective crystal dissolution, *Contrib. Mineral. Petrol.*, *121*, 237–246, doi:10.1007/BF02688239.

Knesel, K. M., J. P. Davidson, and W. A. Duffield (1999), Evolution of silicic magma through assimilation and subsequent recharge: Evidence from Sr isotopes in sanidine phenocrysts, Taylor Creek Rhyolite, NM, *J. Petrol.*, *40*, 773–786, doi:10.1093/petrology/40.5.773.

Larsen, J. F. (2005), Experimental study of plagioclase rim growth around anorthite seed crystals in rhyodacitic melt, *Am. Mineral.*, *90*, 417–427, doi:10.2138/am.2005.1456.

Liang, Y. (2000), Dissolution in molten silicates: Effects of solid motion, *Geochim. Cosmochim. Acta*, *64*, 1617–1627, doi:10.1016/S0016-7037(00)00331-8.

Liang, Y. (2003), Kinetics of crystal-melt reaction in partially molten silicates: 1. Grain scale processes, *Geochem. Geophys. Geosyst.*, *4*(5), 1045, doi:10.1029/2002GC000375.

Linden, P. F., and J. M. Redondo (1991), Molecular mixing in Rayleigh-Taylor instability. Part I: Global mixing, *Phys. Fluids A*, *3*, 1269–1277, doi:10.1063/1.858055.

Longo, A., M. Vassalli, P. Papale, and M. Barsanti (2006), Numerical simulation of convection and mixing in magma chambers replenished with CO_2-rich magma, *Geophys. Res. Lett.*, *33*, L21305, doi:10.1029/2006GL027760.

Marsh, B. D. (1988), Crystal capture, sorting, and retention in convecting magma, *Geol. Soc. Am. Bull.*, *100*, 1720–1737, doi:10.1130/0016-7606(1988)100<1720:CCSARI>2.3.CO;2.

Marsh, B. D. (1989), On convective style and vigor in sheet-like magma chambers, *J. Petrol.*, *30*, 479–530.

Maxey, M. R., and J. J. Riley (1983), Equation of motion for a small rigid sphere in a nonuniform flow, *Phys. Fluids*, *26*, 883–889, doi:10.1063/1.864230.

Morgan, D. J., D. A. Jerram, D. G. Chertkoff, J. P. Davidson, D. G. Pearson, A. Kronz, and G. M. Nowell (2007), Combining CSD and isotopic microanalysis: Magma supply and mixing processes at Stromboli Volcano, Aeolian Islands, Italy, *Earth Planet. Sci. Lett.*, *260*, 419–431, doi:10.1016/j.epsl.2007.05.037.

Nakamura, M. (1995), Continuous mixing of crystal mush and replenished magma in the ongoing Unzen eruption, *Geology*, *23*, 807–810, doi:10.1130/0091-7613(1995)023<0807:CMOCMA>2.3.CO;2.

Namiki, A., and M. Manga (2006), Influence of decompression rate on the expansion velocity and expansion style of bubbly fluids, *J. Geophys. Res.*, *111*, B11208, doi:10.1029/2005JB004132.

Nitsche, J. M., and G. K. Batchelor (1997), Break-up of a falling drop containing dispersed particles, *J. Fluid Mech.*, *340*, 161–175, doi:10.1017/S0022112097005223.

Oldenburg, C. M., F. J. Spera, D. A. Yuen, and G. Sewell (1989), Dynamic mixing in magma bodies: Theory, simulations and implications, *J. Geophys. Res.*, *94*, 9215–9236, doi:10.1029/JB094iB07p09215.

Ottino, J. M. (1990), Mixing, chaotic advection, and turbulence, *Annu. Rev. Fluid Mech.*, *22*, 207–253, doi:10.1146/annurev.fl.22.010190.001231.

Pallister, J. S., R. P. Hoblitt, and A. G. Reyer (1992), A basalt trigger for the 1991 eruption of Pinatubo volcano?, *Nature*, *356*, 426–428, doi:10.1038/356426a0.

Patankar, S. V. (1980), *Numerical Heat Transfer and Fluid Flow*, 210 pp., Hemisphere, Washington, D. C.

Phillips, J. C., and A. W. Woods (2001), Bubble plumes generated during recharge of basaltic magma reservoirs, *Earth Planet. Sci. Lett.*, *186*, 297–309, doi:10.1016/S0012-821X(01)00221-7.

Ramaprabhu, P., and M. J. Andrews (2004), Experimental investigation of Rayleigh-Taylor mixing at small Atwood numbers, *J. Fluid Mech.*, *502*, 233–271, doi:10.1017/S0022112003007419.

Ramberg, H. (1981), *Gravity, Deformation, and the Earth's Crust, in Theory, Experiments and Geological Application*, 452 pp., Academic, London.

Ruprecht, P., and G. Wörner (2007), Variable regimes in magma systems documented in plagioclase zoning patterns: El Misti stratovolcano and Andahua monogenetic cones, *J. Volcanol. Geotherm. Res.*, *165*, 142–162, doi:10.1016/j.jvolgeores.2007.06.002.

Scaillet, B., F. Holtz, and M. Pichavant (1998), Phase equilibrium constraints on the viscosity of silicic magmas: 1. Volcanic-plutonic comparison, *J. Geophys. Res.*, *103*, 27,257–27,266, doi:10.1029/98JB02469.

Shaw, C. S. J. (2006), Effects of melt viscosity and silica activity on the rate and mechanism of quartz dissolution in melts of the CMAS and CAS systems, *Contrib. Mineral. Petrol.*, *151*, 665–680, doi:10.1007/s00410-006-0086-3.

Singer, B. S., M. A. Dungan, and G. D. Layne (1995), Textures and Sr, Ba, Mg, Fe, K, and Ti compositional profiles in volcanic plagioclase: Clues to the dynamics of calc-alkaline magma chambers, *Am. Mineral.*, *80*, 776–798.

Snyder, D. (2000), Thermal effects of the intrusion of basaltic magma into a more silicic magma chamber and implications for eruption triggering, *Earth Planet. Sci. Lett.*, *175*, 257–273, doi:10.1016/S0012-821X(99)00301-5.

Snyder, D., and S. Tait (1996), Magma mixing by convective entrainment, *Nature*, *379*, 529–531, doi:10.1038/379529a0.

Spera, F. J. (1984), Some numerical experiments on the withdrawal of magma from crustal reservoirs, *J. Geophys. Res.*, *89*, 8222–8236, doi:10.1029/JB089iB10p08222.

Syamlal, M., W. Rogers, and T. J. O'Brien (1993), *MFIX Documentation: Theory Guide*, *Tech. Note DOE/METC-94/1004*, 49 pp., U.S. Dep. of Energy, Morgantown, W. Va.

Tepley, F. J., III, J. P. Davidson, R. I. Tilling, and J. G. Arth (2000), Magma mixing, recharge and eruption histories recorded in plagioclase phenocrysts from El Chichon Volcano, Mexico, *J. Petrol.*, *41*, 1397–1411, doi:10.1093/petrology/41.9.1397.

Trial, A. F., F. J. Spera, J. Greer, and D. A. Yuen (1992), Simulations of magma withdrawal from compositionally zoned bodies, *J. Geophys. Res.*, *97*, 6713–6733, doi:10.1029/91JB03130.

Vazquez, J. A., and M. R. Reid (2004), Probing the accumulation history of the voluminous Toba Magma, *Science*, *305*, 991–994, doi:10.1126/science.1096994.

Wallace, G. S., and G. W. Bergantz (2005), Reconciling heterogeneity in crystal zoning data: An application of shared characteristic diagrams at Chaos Crags, Lassen Volcanic Center, California, *Contrib. Mineral. Petrol.*, *149*, 98–112, doi:10.1007/s00410-004-0639-2.

Watson, E. B. (1994), Diffusion in volatile-bearing magmas, in *Volatiles in Magmas*, *Rev. Mineral. Geochem.*, vol. 30, edited by M. R. Carroll and J. R. Holloway, pp. 372–411, Mineral. Soc. of Am., Washington, D. C.

Wolf, A., J. B. Swift, H. L. Swinney, and J. A. Vastano (1985), Determining Lyapunov exponents from a time series, *Phys. D*, *16*, 285–317, doi:10.1016/0167-2789(85)90011-9.

Youngs, D. L. (1984), Numerical simulation of turbulent mixing by Rayleigh-Taylor instability, *Phys. D*, *12*, 32–44, doi:10.1016/0167-2789(84)90512-8.

Zellmer, G. F., R. S. J. Sparks, C. J. Hawkesworth, and M. Wiedenbeck (2003), Magma emplacement and remobilization timescales beneath Montserrat: Insights from Sr and Ba zonation in plagioclase phenocrysts, *J. Petrol.*, *44*, 1413–1431, doi:10.1093/petrology/44.8.1413.

Zhang, Y., D. Walker, and C. E. Lesher (1989), Diffusive crystal dissolution, *Contrib. Mineral. Petrol.*, *102*, 492–513, doi:10.1007/BF00371090.